Stress Distributions in Plasma-Sprayed Thermal Barrier Coatings under Thermal Cycling in a Temperature Gradient

Andi M. Limarga[a,*], Robert Vaßen[b] and David R. Clarke[a]

[a] School of Engineering and Applied Sciences, Harvard University, Cambridge, MA 02138
[b] Forschungszentrum Juelich GmbH, Germany

[*] Email: limarga@seas.harvard.edu

Abstract

The residual stress distribution in plasma-sprayed zirconia thermal barrier coatings subjected to cyclic thermal gradient testing was evaluated using Raman piezospectroscopy and finite element computation. Thermal gradients of 440°C/mm were achieved by flame heating the front of a PS coating and cooling the metal backside with compressed air. The thermal gradient testing, performed in the Juelich test, consisted of repeated front-side heating with a flame and constant cooling of the back-side of the metal substrate with either front side radiative cooling or forced air cooling between the heating cycles. The coatings exhibited characteristic "mud-cracking" with the average crack spacing dependent on the cooling treatment. This is consistent with finite element calculations and Raman spectroscopy measurements in which the sudden drop in coating surface temperature on initial cooling leads to a large biaxial tension at the surface. Key to the proper interpretation of the Raman shifts is that the stress-free Raman peaks need to be corrected for shifts associated with the evolution of the metastable tetragonal phase with aging.

Keywords: thermal barrier coating, Raman spectroscopy, residual stress, thermal gradient

1. Introduction

The primary functional role of thermal barrier coatings (TBCs) is to enable the gas temperature (T4) in the hottest portion of turbines to be substantially higher than the maximum surface temperature of the bare metallic blades and vanes would otherwise allow [1-2]. This is achieved by internal cooling of the blades and vanes with the outer surface of the thermal barrier coatings being exposed to the hot gases. The TBC provides the thermal insulation and so, consequently, thermal barrier coatings are always used in a temperature gradient. While substantial progress has been made in identifying failure modes under isothermal cyclic tests, in which there is no temperature gradient, and relating the modes to various properties of the TBC and underlying bond-coat alloys [3-6] there remains a paucity of knowledge of failure mechanisms under thermal gradient conditions. (Because the thermal gradients can be large in engines, cyclic testing is generally performed in burner rigs.) The transient stresses are also more complicated under cyclic temperature gradient tests since the stresses vary with position as well as temperature in the coating [7], so greater reliance has to be placed on finite element calculations of the temperature and stress distributions. To validate the predictions of the calculations, high resolution measurements of the stresses in the coating are needed.

Unfortunately, the measurement of stresses in coatings has not been well established and the majority of techniques that have been applied, namely x-ray diffraction [8-9], neutron diffraction [10-11], curvature measurement [12-13] and layer-by-layer removal method [13-14] produce an average stress in the coating and are not able to reveal the stress distribution through the coating. High spatial resolution X-ray diffraction using intense long wavelength X-rays, such as those at synchrotrons, offer considerable potential but the application of these methods to actual components is rather difficult or, in some cases, impractical. For this reason, a number of groups have used Raman piezospectroscopy since it offers a significant advantage in that it can be localized by using a focused laser probe and hence, can be used to resolve the stress distribution in the coating due to its high spatial resolution (of the order of 1 μm). Although these have been performed at room temperature, they can be also be carried out at high temperature with appropriate instrumentation. However, there is reason to doubt the

actual numerical values of the stresses reported since it has been assumed that the stress-free lattice parameters of zirconia are constant, irrespective of the length of time and temperature that the zirconia has been exposed to.

The difficulty arises because the majority of current thermal barrier coatings are made of the metastable tetragonal phase of yttria-stabilized zirconia. Over prolonged, high-temperature exposure, the yttria ions partition by diffusion in the metastable phase to produce a two-phase mixture of equilibrium tetragonal and cubic phases, each with its own lattice parameter [15]. Thus, the stress-free lattice parameter varies with aging. Taken together with the variation in temperature through a coating in a gradient, this further complicates the derivation of the stress distribution. As will be shown in this work, this affects the values of the stresses derived from the measurements.

2. Experimental details

2.1. Specimen and thermal cycling setup

The material investigated consisted of an IN-738 nickel-based superalloy substrate (3 mm thick, 25.4 mm diameter) coated with 150 μm thick NiCoCrAlY bond coat deposited using vacuum plasma spray and a 500 μm thick air plasma sprayed top coat of 8 wt. % yttria stabilized zirconia (8YSZ). The coatings were applied at FZ Juelich. Prior to deposition, the substrates were grit-blasted to improve the coating adhesion. A typical microstructure of the coating in its as-sprayed condition is shown in Figure 1.

Cyclic thermal gradient experiments were performed at FZ Juelich using an experimental setup shown in Figure 2 and described in detail elsewhere [16]. The temperature of the TBC outer surface was measured with an infra-red pyrometer while the temperature in the middle of the metallic substrate thickness was measured using a K-type thermocouple. The thermal cycle used consisted of a 1-minute heating, 4-minute high-temperature hold followed by a 1-minute cooling periods (Figure 3). During the heating and holding periods, the front side of the specimen (the top of the TBC) was heated using a natural gas/oxygen burner while the back

side was cooled with compressed air. At the end of the high temperature hold, the burner was rapidly moved away from the specimen while the cooling of the back side was continued. A total of 400 cycles was performed on the specimens before they were removed from the thermal cycling rig. In another set of experiment, an identical cyclic thermal gradient was performed for 399 cycles. In the last cycle (cycle #400), the front side cooling was augmented using compressed air. This treatment resulted in a different cooling scenario, one in which the surface of the TBC cools faster than the interior (Figure 3).

2.2. Raman spectroscopy

Raman spectra were recorded on cross-sections cut of the specimens after they were mounted in epoxy to ensure that the coating remained intact. The measurements were made using 633-nm laser excitation in a confocal Raman microprobe (LabRAM Aramis, Horiba Jobin Yvon, Edison, NJ). Raman spectra were acquired as a function of distance in the cross-sections from the outer surface of the TBC and the results reported in this study were the average and standard deviation from 10 different locations at the same distance from the top surface. The peak positions of each spectrum were then obtained through a deconvolution procedure using commercial peak-fitting software (GRAMS, Thermo Electron Corp., Philadelphia, PA) assuming mixed Lorentzian and Gaussian profiles for Raman lines at 465, 610 and 640 cm^{-1}. The other characteristic Raman lines of tetragonal zirconia at 145, 260 and 320 cm^{-1} are asymmetric and hence, fitted using Breit-Wigner profile (an asymmetric Lorentzian function) [15] using OriginPro package (OriginLab Corp., Northampton, MA). A typical example of this curve-fitting procedure is shown in Figure 4 with the deconvoluted peaks also indicated. In previous Raman piezo-spectroscopy measurements of residual stress distribution in tetragonal-zirconia thermal barrier coatings, the shift of the Raman peak at around 640 cm^{-1} was used since it has a good signal to noise ratio [13, 17-19]. However, our recent study on piezo-spectroscopy of tetragonal zirconia indicated that the peak at 465 cm^{-1} is more suitable for stress measurement due to its larger piezospectroscopic constant, making it more sensitive to stress [20]. Furthermore, this peak is well isolated from the other Raman peaks, resulting in a smaller

uncertainty in the curve fitting process and hence more precise determination of the peak frequency.

To correct for possible shifts of the stress-free position of the Raman peak due to the evolution of the metastable phase with time at temperature, small pieces of as-sprayed coating (approximately 2mm^2 in area) were scraped off and each annealed in air at different temperatures for 27 hours. The temperatures selected, from 1050°C up to 1350°C, were to replicate the temperatures at various locations in the coating during thermal cycling while the duration of the annealing corresponded to the total accumulated time of the coating at temperature during thermal cycling.

2.3. Raman piezospectroscopy

The evaluation of stresses by Raman piezospectroscopy relies on the measurement of the shift of Raman lines relative to their unstrained state. In the linear elastic regime, the change in frequency, $\Delta \nu$, is related to the stress tensor by the relationship:

$$\Delta \nu = \nu - \nu_0 = \Pi_{ij} \sigma_{ij} \tag{1}$$

where $\Delta \nu$ refers to the frequency shift from the stress-free state (ν_0), Π_{ij} is the piezospectroscopic (PS) tensor, and σ_{ij} is the stress tensor (suffixes are written according to the repeated index notation). In polycrystalline materials with no crystallographic texture, Eq. (1) reduces to the simpler form

$$\Delta \nu = \Pi \langle \sigma \rangle \tag{2}$$

where Π and $\langle \sigma \rangle$ are the trace of the PS constants and the spatial average stress tensor, respectively. Strictly speaking, the Raman peak shift is influenced by the strain (rather than stress) in the material. The piezospectroscopic constant for dense tetragonal-zirconia was measured under uniaxial stress and it was found to be 2.01 cm^{-1}/GPa for the Raman peak at 465

cm^{-1} [20]. To obtain the strain distribution in the coating, the stress-based PS constant can be converted to strain-based constant with a simple relationship:

$$\Pi(\varepsilon) = \frac{E}{1 - 2\nu_n} \Pi(\sigma) \qquad (3)$$

where $\Pi(\varepsilon)$ and $\Pi(\sigma)$ are strain-based and stress-based PS constants, respectively. E and ν_n are the elastic modulus and Poisson's ratio of the material. Assuming E = 200 GPa and ν = 0.2 for dense zirconia, the strain-based PS constant, $\Pi(\varepsilon)$ is 670 cm^{-1} (per unit strain). It is emphasized that the strain calculated from Raman peak shift refers to the trace of strain tensor $\varepsilon_{ii} = (\varepsilon_{11} + \varepsilon_{22} + \varepsilon_{33})$.

3. Finite element calculations

To evaluate the temperature and thermal stress distribution within the coating during thermal cycling with a temperature gradient, finite element analysis was performed using the ABAQUS code (Simulia, Providence, RI, USA). An axi-symmetric model used in the analysis represents the thermal barrier coated superalloys with identical geometry and dimension mentioned above. For simplicity, all interfaces (TBC/bond coat, bond coat/TGO and TGO/superalloys) were assumed to be flat and have perfect bonding. Furthermore, stress relaxation due to cracking was not taken into consideration. However, creep processes and plasticity (particularly at high temperature) were included in the analysis. The temperature-dependent material properties used in the finite element simulation were obtained from Refs. [21-26] and are listed in Table 1. Pertinent to comparison with Raman spectroscopy, the elastic modulus of plasma-sprayed zirconia was assumed to be 50 GPa. The creep behavior of the bond coat, TGO and the TBC layer was assumed to follow a Norton power-law equation $\dot{\varepsilon} = A\sigma^n \exp(-Q/RT)$ and their parameters were listed in Table 2.

Heating and cooling were simulated by applying heat convection as the boundary conditions on the TBC surface and the back side of the metal. In the calculations, the

convection coefficients and gas temperature were adjusted so that the simulated thermal history matched the measurements of the difference in temperature between the TBC surface and the mid-point of the superalloy substrate (Figure 5).

4. Results

4.1. Microstructural observation on TBC surface cracking

Observation on the surface of the TBC after planarizing by polishing showed that the coatings all developed a network of surface cracks, commonly referred to as mud-cracking (Figure 6). These cracks are not visible without first polishing the top of the coating to remove its roughness. The crack spacing varies from 500 μm in the coating cooled from the back side down to 100-250 μm in the coating cooled from both sides. The presence of cracks perpendicular to the coating surface/interface indicated that the coating surface had been subjected to a large in-plane tensile stress [7] during the tests. The origin of the stresses is described in the following section.

4.2. Finite element analysis of the stress evolution in the coating

Figure 7 shows the evolution of in-plane stresses in the coatings subjected to the two different last thermal cycles. For ease of presentation and comparison, we have selected three planes in the coating namely the TBC outer surface, the midpoint (halfway through its thickness) and at the TBC/TGO interface. The heating and holding segments are identical, as expected since they were the same for all the samples, with the differences occurring during cooling. During the initial part of heating, the temperature at the top surface of the TBC increases much faster than the coating interior, leading to a differential expansion of the coating, depending on the location. This difference leads to the generation of a compressive stress on the coating surface since the hotter surface is constrained by the cooler, inner parts of the coating and alloy. As the heating continues and heat diffuses in from the surface, the temperatures in the coating interior and in the underlying metallic substrate increase so that

the compressive stress at the surface decreases. In contrast, the coating near the TBC/TGO interface is subjected to tensile stress almost immediately which continues to increase throughout the heating portion of the cycle. Once the maximum temperature is reached and during high-temperature hold, the stresses in the coating are relaxed by creep deformation. By the end of the four minute hold, the coating is almost stress-free except for near its interface with the metallic bond coat alloy.

During the earliest part of the cooling, once the heating flame is removed the temperature of the TBC surface drops abruptly as shown in the temperature data in figure 3. More striking is the sudden change in the temperature difference between the coating outer surface and the mid-point temperature in the alloy. At the end of the high-temperature hold, the temperature difference between the outer surface and the TBC/TGO interface was 304°C. During the first two seconds of the cooling, this temperature difference dropped to 23°C in the case of coating cooled from the back side only and to minus 208°C, meaning that the top surface of the coating was 208°C cooler than the metal, when forced cooled from both sides. Such temperature drops lead to the generation of significant tensile in-plane stress at the coating surface: 206 MPa and 375 MPa in the coating cooled only from the back side and in the coating cooled from both sides, respectively. During subsequent cooling, the tensile stress in the coating decreases and then becomes compressive due to the higher thermal expansion of the thick metal substrate.

4.3. Residual stress measurement by Raman spectroscopy

4.3.1. Stress-free Raman peak shift in yttria-stabilized zirconia with aging

The position and width (full width at half maximum) of the Raman peak at around 465 cm^{-1} after aging the scraped powders at various temperatures are shown in Figure 8.   With aging at higher temperatures, the Raman peak shifted to a lower wavenumber and the peak underwent significant sharpening.   The sharpening of Raman bands has been observed previously in yttria-stabilized zirconia coating deposited by electron beam physical vapor

deposition process [15] and has been attributed to decreasing anion disorder upon aging and phase evolution. Recently, we have also shown that the sharpening and peak shift of the Raman bands occurs in metastable tetragonal zirconia powders and coatings with various compositions and microstructure [27]. The shifts shown in figure 8 are commensurate with these complementary measurements.

4.3.2. Raman peak shift and strain distribution in thermal barrier coatings with different cooling scenarios

The frequency of the Raman band at 465 cm^{-1} measured at various locations within the coatings for the two cooling scenarios are shown in Figure 9. Two specimens with back side forced cooling only (Figure 9a) and one specimen with back and front side forced cooling (Figure 9b) were examined. Also plotted in Figure 9 is the temperature-dependent strain-free peak position determined from the calculated temperatures and the strain-free Raman data from the aging calibration shown in Figure 8. This has been converted to position-dependent peak position using the calculated temperature profile from finite element analysis. In the specimens forced cooled only from the back side, the Raman peak near the surface of the coating has shifted to a lower wavenumber (~463.8 cm^{-1}) compared to that near the TBC/TGO interface (~465.3 cm^{-1}). Nevertheless, the two specimens evaluated in this study indicated that the peak shift is rather close to that without any stress. One specimen showed a lower wavenumber than the strain-free annealing (indicating tensile residual stress) and the other showed a higher wavenumber (compressive residual stress). In contrast, the frequencies of the Raman peaks recorded from different depths in the coating force cooled from both sides in the last cycle shifted to a higher wavenumber in most locations, indicating that the residual stress in that coating is mainly compressive. From this data, the calculated strain distributions in the coatings are shown in Figure 10 after correcting for the frequency shift due to aging. These indicate that the strains in the coatings cooled only from the back side are rather low and almost strain-free, generally within 5 x 10^{-4} of being strain free. One coating showed a slight tensile net strain throughout while the other was slightly compressive except right at the outer surface. The strains in the coating force cooled from both sides, however, are compressive

throughout almost the entire thickness switching to tensile strain adjacent to the TBC/TGO interface.

4.4. Comparison between measured and calculated stress distributions

Although the Raman frequency shifts are measures of strains, it is more convenient and conventional to compare the Raman measurements with the finite element analyses in term of in-plane stress. However, the conversion of Raman peak frequency shifts measured on a cross-section to the in-plane stress in an intact coating prior to sectioning involves several assumptions and uncertainties. Typically, it is assumed that the coating is significantly thinner than the metal substrate and all interfaces are considered flat so that the normal stress to the coating surface is zero. This assumption leads to the coating being under biaxial stress, σ_B. Cutting the specimen to produce a cross-section introduces a new surface which is traction free and so the stress component normal to the cutting plane which was a component of the biaxial stress state now becomes zero at the surface and builds up again going into the coating below the sectioned plane. The biaxial stress σ_B in the coating prior to sectioning can be calculated from the Raman peak shift $\Delta \nu$ as follows:

$$\sigma_B = \frac{1 - \nu_n}{\Pi} \frac{E_{TBC}}{E_{dense}} \Delta \nu$$

(4)

where ν_n is the Poisson's ratio, E_{TBC}/E_{dense} is the ratio between elastic modulus of the coating and that of dense material. Π is the piezospectroscopic constant of the dense material obtained under uniaxial stress.

Figure 11 shows the stresses calculated using finite element analysis and those obtained from Raman piezospectroscopy based on the above assumption. The calculated stresses at high temperature refer to those generated during instantaneous cooling of the TBC top surface before the entire coating/metal system cools down to room temperature. The sudden cooling of the TBC surface leads to a stress gradient in the coating where the coating surface is subjected to tensile stresses. Assuming a linear fit to the stress profiles in Figure 11, the stress

gradients in the coatings predicted by finite element analysis are -0.18 and -0.48 MPa/μm for the coating cooled from the back side and from both sides, respectively. These values are lower than those calculated using Evans and Hutchinson's model [7], which are -0.35 and -0.64 MPa/μm. This discrepancy is a result of the different stress distribution in the coating prior to cooling. In their analysis, Evans and Hutchinson assumed that the coating is stress-free[7] and elastic while our finite element simulation indicated that stress created by the rapid heating is not fully relaxed by creep and plastic deformation in the four minute hold at high temperature. During subsequent cooling to room temperature, the contraction of the underlying superalloys dominates and the stresses become compressive. In the coatings cooled only from the back side, the measured stresses near the TBC surface were about 20-40 MPa but the average stress in the interior of the coatings were essentially zero. The measured residual stress in the coating cooled from both sides is mainly compressive with a maximum of approximately -100 MPa. The stress is slightly tensile near the TBC/TGO interface.

5. Discussion

The observations described in this work indicate the cooling conditions applied to a thermal barrier coated system when subject to thermal cycling under a temperature gradient can dramatically affect the stress distribution in the coating. If the surface cooling is sufficiently rapid, cracking can initiate at the surface. In turn, this can modify the residual stress distribution in the coating at room temperature and measured by techniques, such as Raman spectroscopy and X-ray diffraction, that might be used to validate finite element analyses of the stresses. In the following, we discuss the stress evolution in the coatings and its effect on the crack formation. Stress measurement by Raman piezospectroscopy is then revisited to highlight some appropriate considerations that must be taken to obtain reliable measurements.

5.1. Mechanism of cracking at the coating surface

As mentioned earlier, the mud-cracking pattern observed in the coating provides direct evidence for the existence of tensile stresses at the coating surface at some stage in the

thermal cycling test. The crack spacing, s, in the coating can be used to estimate the magnitude of the tensile stress, σ_B, according to the following relationship [28]:

$$\sigma_B = \left\{ \frac{\Gamma_{TBC}\bar{E}_{TBC}}{\ell\left[2\tanh\left(\dfrac{s}{2\ell}\right) - \tanh\left(\dfrac{s}{\ell}\right)\right]} \right\}^{0.5} \tag{5}$$

with $\bar{E}_{TBC} = \dfrac{E_{TBC}}{1 - v_{TBC}^2}$ and $\ell = \dfrac{\pi}{2}g(D)h$

where E_{TBC}, v_{TBC} and Γ_{TBC} are the elastic modulus, Poisson's ratio and fracture toughness of the TBC, respectively. h is the coating thickness and $g(D)$ is a parameter dependent on the Dundurs parameter $D = \dfrac{\bar{E}_{TBC} - \bar{E}_{sub}}{\bar{E}_{TBC} + \bar{E}_{sub}}$, and plotted in [28]. For the elastic properties considered in this work, the Dundurs parameter is equal to -0.5 so that $g(D) \cong 1$ [28]. The fracture toughness of the APS TBC is approximately 30 Jm^{-2} [29]. Equation (5) predicts a tensile stress in the range of 189 to 499 MPa for the coating cooled only from the back side with a crack spacing of approximately 250-500 μm, and a tensile stress of 499 up to 1097 MPa for the coating cooled from both sides (with a crack spacing of 150-250 μm).

Finite element analysis showed that the coating surface exhibited a large in-plane tensile stress during the initial transient cooling, when the temperature of the surface dropped due to the sudden cooling (Figure 7). The tensile stress was generated because of the differential contraction between the coating surface and the coating interior (and the underlying metal). The coating cooled from both sides experienced a temperature drop of 512°C while the surface temperature of the coating cooled only from the back side dropped by 281°C. In the elastic regime, the magnitude of the stress is proportional to the temperature drop ΔT [7]:

12

$$\sigma_B = \frac{E_{TBC}\,\alpha_{TBC}\,\Delta T}{1-\nu_{TBC}} \tag{6}$$

where α_{TBC} is the thermal expansion coefficient of the coating. The calculated stresses associated with this sudden cooling were 206 MPa for the coating cooled only from the back side and 375 MPa for the coating cooled from both sides. The reasonable agreement, at least qualitatively, between the stresses estimated from the average crack spacing and those calculated by finite element analysis suggests that the coating surface cracks during the transient cooling period. On further cooling to room temperature, finite element analysis shows that the continued contraction of the underlying metallic substrate puts the coatings, in both cases, under compression.

5.2. Limitation of the finite element analysis

Raman measurement indicated that the measured stresses in the coating are smaller than those predicted by finite element analysis. In both cases, finite element analysis suggested that the residual stresses in the coatings are compressive. However, while the experimental measurement showed that the stresses in the coating cooled from both sides were compressive, the measured stress in the coating cooled only from back side was essentially zero. To understand this discrepancy, we have outlined the limitations of the finite element modeling performed in this study.

The first simplification made in this study was that the coating was homogeneous and that only one thermal cycle was simulated in the finite element analysis. It was assumed that the accumulated stresses in the coatings in the previous cycles were completely relaxed by various stress relaxation mechanisms. The analysis considered the last cycle of the cyclic thermal gradient experiment under two different cooling scenarios. This simplified analysis was able to capture an important event during cooling process, namely the generation of tensile stress at the coating surface as the surface of the coating cools faster than the interior. There is also qualitative agreement between the stresses estimated by finite element analysis and those calculated from the crack spacing. However, the density of the cracks observed after the

thermal cycling may also be an overestimate due to the crack accumulation sometime during the previous 399 thermal cycles, not considered in the analysis.

The formation and propagation of these vertical cracks have two major consequences that were not considered in the present finite element analysis. Firstly, cracking releases some of the stress in the coating. Hence, it is reasonable to expect that the measured stresses are lower than the predicted values. Secondly, cracking also alters the elastic modulus of the coating. As the cracks initiated from the coating surface and propagated towards the interface due to the in-plane tensile stress, the elastic modulus of the coating is no longer constant. Rather, the elastic modulus would be dependent on the location within the coating because of the presence of surface cracks.

Lastly, the effect of sintering has also been neglected in the finite element analysis, largely because very little is known about its constitutive behavior. Sintering is a temperature-dependent process and, hence, is position-dependent in a thermal gradient condition: sintering occurs at a higher rate at the surface compared to sintering near the TBC/TGO interface. Sintering of the coating increases the thermal conductivity of the coating, redistributes the stress and more importantly, can be expected to increase the elastic modulus of the coating. Here, the elastic modulus of the coating near the surface will be higher than that near the TBC/TGO interface. Such a competition between elastic modulus decrease due to cracking and increase due to sintering is rather complex and beyond the scope of this study.

5.3. Considerations for stress measurement by Raman piezo-spectroscopy

The application of Raman piezospectroscopy to quantify residual stresses in zirconia coatings has been hindered by the difficulty in interpreting the Raman peak shifts and converting them to residual stress. Here we highlight some crucial considerations in the stress measurement by Raman spectroscopy to ensure the accuracy of the measurement.

The calculation of stress from Raman spectroscopy relies on the accurate determination of the strain-free Raman position. Previously, the stress-free Raman position was considered only to be composition dependent. This study, along with our recent work however, shows that the peak position also depends on the thermal history of the material (temperature and

duration of high-temperature aging). For example, the Raman peak at 465 cm^{-1} shifts to a lower wavenumber with increasing aging temperature and time [27]. In a thermal barrier coating subjected to a thermal gradient, this leads to the stress-free Raman peak position being dependent on the location within the coating, as shown in Figure 8. In the coatings investigated in this study, this resulted in a small value for the stress in the coatings. To illustrate the importance of this aging dependence on Raman shift, we also assessed the stresses in the coatings assuming a constant stress-free Raman peak position (Figure 12). These calculations suggest that the coatings cooled only from the back side exhibited large tensile stresses at the coating surface while the coating near the interface was almost stress-free. In contrast, the coating cooled from both sides appeared to have small tensile stress throughout the coating. Such assessments are quite different from the stress calculation using the corrected temperature-dependent stress free Raman shift. Furthermore, without this correction the calculated tensile stress throughout the entire coating is inconsistent with the finite element analysis, as well as intuition, which shows that the coating will go into compression at room temperature due to the contraction of the more massive, underlying metal. A similar correction to account for phase partitioning should also be made in quantifying the residual stresses by X-ray diffraction.

6. Conclusion

The residual stress in plasma-sprayed zirconia thermal barrier coatings subjected to cyclic thermal gradient has been evaluated using finite element analysis and Raman piezo-spectroscopy. Microstructural observation revealed that the coating exhibited mud-cracking, with the crack spacing controlled by the cooling rate of the coating. Finite element simulation showed that the temperature of the coating surface dropped rapidly, leading to large in-plane tensile stresses at the surface. The magnitude of the stress depends on the cooling rate during thermal cycling: coatings cooled from both sides experienced larger temperature drops and hence, larger tensile stress than coatings cooled only from the back side. As a result, the crack density is higher in the coating cooled from both sides. Due to cracking, the residual stresses

measured by Raman spectroscopy were low, on the order of -20 up to 40 MPa in the coatings cooled only from the back side and -100 up to 50 MPa in the coating cooled from both side at the last cycle of the thermal cycling.

We have also shown that the stress-free Raman peak position, which is crucial in the stress determination, evolves with high-temperature aging. In particular, the position of Raman peak at 465 cm^{-1} shifts to a lower wavenumber when the coating is aged at a higher temperature. This is crucial when the coating is subjected to prolonged thermal gradient exposure as the stress-free Raman position depends on the location within the coating. Failure to recognize this stress-free peak shift results in erroneous values and, as shown in this work, may lead to incorrect conclusions regarding the stress distribution in coatings subject to exposure in a thermal gradient.

Acknowledgement

References

[1]   Clarke DR, Levi CG. Materials designs for the next generation thermal barrier coatings. Annual Review of Materials Research 2003;33:383.
[2]   Levi CG. Emerging materials and processes for thermal barrier systems. Current Opinion in Solid State and Materials Science 2004;8:77.
[3]   Evans AG, Mumm DR, Hutchinson JW, Meier GH, Pettit FS. Mechanisms controlling the durability of thermal barrier coatings. Progress in Materials Science 2001;46:505.
[4]   Christensen RJ, Lipkin DM, Clarke DR, Murphy KS. Nondestructive evaluation of the oxidation stresses through thermal barrier coatings using Cr^{3+} piezospectroscopy. Applied Physics Letters 1996;69:3754.
[5]   Paton NE, Murphy KS, Clarke DR. Thermal barrier coating stress measurement. 2000.
[6]   Gell M, Sridharan S, Wen M, Jordan EH. Photoluminescence piezospectroscopy: a multi-purpose quality control and NDI technique for thermal barrier coatings. International Journal of Applied Ceramic Technology 2004;1:316.

[7]   Evans AG, Hutchinson JW. The mechanics of coating delamination in thermal gradients. Surface and Coatings Technology 2007;201:7905.

[8]   Scardi P, Leoni M, Bertamini L. Influence of phase stability on the residual stress in partially stabilized zirconia TBC produced by plasma spray. Surface and Coatings Technology 1995;76:106.

[9]   Levit M, Grimberg I, Weiss B-Z. Residual stresses in ceramic plasma-sprayed thermal barrier coatings: measurement and calculation. Materials Science and Engineering A 1996;206:30.

[10]   Kesler O, Matejicek J, Sampath S, Suresh S, Gnaeupel-Herold T, P.C. Brand, Prask HJ. Measurement of residual stress in plasma-sprayed metallic, ceramic and composite coatings. Materials Science and Engineering A 1998;257:215.

[11]   Matejicek J, Sampath S, Brand PC, Prask HJ. Quenching, thermal and residual stress in plasma sprayed deposits: NiCrAlY and YSZ coatings. Acta Materialia 1999;47:607.

[12]   Hobbs MK, Reiter H. Residual stresses in ZrO_2-8%Y_2O_3 plasma-sprayed thermal barrier coating. Surface and Coatings Technology 1988;34:33.

[13]   Teixeira V, Andritschky M, Fischer W, Buchkremer HP, Stover D. Analysis of residual stresses in thermal barrier coatings. Journal of Materials Processing Technology 1999;92-93:209.

[14]   Greving DJ, Rybicki EF, Shadley JR. Through-thickness residual stress evaluations for several industrial thermal spray coatings using a modified layer-removal method. Journal of Thermal Spray Technology 1994;3:379.

[15]   Lughi V, Clarke DR. Transformation of electron-beam physical vapor-deposited 8 wt% yttria-stabilized zirconia thermal barrier coatings. Journal of the American Ceramic Society 2005;88:2552.

[16]   Traeger F, Vassen R, Rauwald K, Stover D. Thermal cycling setup for testing thermal barrier coatings. Advanced Engineering Materials 2003;5:429.

[17]   Portinha A, Teixeira V, Carneiroa J, Beghi MG, Bottani CE, N NF, R RV, D DS, Sequeira AD. Residual stresses and elastic modulus of thermal barrier coatings graded in porosity. Surface and Coatings Technology 2004;188-189:120.

[18]   Tomimatsu T, Y YK, SJ SJZ. Residual Stress Distribution in Electron Beam–Physical Vapor Deposited ZrO2 Thermal Barrier Coating Layer by Raman Spectroscopy. Metallurgical and Materials Transactions A 2003;34A:1739.

[19]   Tanaka M, Hasegawa M, Dericioglu AF, Kagawa Y. Measurement of residual stress in air plasma-sprayed Y2O3–ZrO2 thermal barrier coating system using micro-Raman spectroscopy. Materials Science and Engineering A 2006;419:262.

[20]   Limarga AM, Clarke DR. Piezo-spectroscopic coefficients of tetragonal-prime yttria-stabilized zirconia. Journal of the American Ceramic Society 2007;90:1272.

[21]   Ahrens M, Lampenscherf S, Vassen R, Stover D. Sintering and creep processes in plasma-sprayed TBCs. Journal of Thermal Spray Technology 2004;13:432.

[22]   Schwarzer J, Vohringer O. High temperature deformation behavior of the bondcoat alloy PWA 1370. Advanced Engineering Materials 2003;5:490.

[23]   Brindley WJ, Whittenberger JD. Stress relaxation of low pressure plasma-sprayed NiCrAlY alloys. Materials Science and Engineering A 1993;163:33.

[24]   DeMasi JT, Sheffler KD, Ortiz M. Thermal barrier coating life prediction model development. Cleveland, OH: NASA Technical Report 182230, 1989.

[25]   Bednarz P. Finite element simulation of stress evolution in thermal barrier coating systems. Institut für Energieforschung (IEF), vol. PhD. Julich: Forschungszentrum Julich GmbH, 2006.

[26]   Busso EP, Qian ZQ, Taylor MP, Evans HE. The influence of bondcoat and topcoat mechanical properties on stress development in thermal barrier coating systems. Acta Materialia 2009;57:2349.

[27]   Limarga AM, Iveland J, Clarke DR. to be submitted.

[28] Xia ZC, Hutchinson JW. Crack patterns in thin films. Journal of the Mechanics and Physics of Solids 2000;48:1107.

[29] Kramer S, Faulhaber S, Chambers M, Clarke DR, Levi CG, Hutchinson JW, Evans AG. Mechanisms of cracking and delamination within thick thermal barrier systems in aero-engines subject to calcium-magnesium-alumino-silicate (CMAS) penetration. Materials Science and Engineering A 2008;490:26.

Figure captions

Figure 1. Cross sectional micrograph of the plasma-sprayed thermal barrier coating in its as-sprayed condition.

Figure 2. Experimental setup of the cyclic thermal gradient experiment.

Figure 3. Measured temperatures of the metal and the coating surface during thermal gradient cycling: (a) with back side cooling and (b) with front side cooling with compressed air. The bottom panel shows the temperature difference between the coating and the metal.

Figure 4. Typical Raman spectrum and peak fitting results from tetragonal zirconia. Residual stress in the coating is determined by evaluating the shift of Raman peak at $465cm^{-1}$.

Figure 5. Temperature difference between the metal and the coating surface measured during experiment with front side cooling and calculated using finite element analysis

Figure 6. Optical micrograph of the coatings after planarizing: (a) in the as-sprayed condition, (b) after thermal cycling with only backside cooling and (c) after thermal cycling with back and front side cooling on the last cycle.

Figure 7. Strain-free position and width of the Raman peak around $465 \ cm^{-1}$ of a fragment of APS TBC annealed for 27 hours at the various temperatures indicated.

Figure 8. Raman peak shift at different location within the coating subjected to cyclic thermal gradient (a) with back side cooling only and (b) with front side cooling on the last cycle. The strain-free peak positions at different locations were calculated by combining the temperature-dependent peak position (shown in Figure 6) and temperature distribution calculated using finite element analysis.

Figure 9. Strain distribution through the coating thickness calculated from the measured Raman peak shift

Figure 10. Evolution of stresses in the coating and the temperature difference between TBC surface and TBC/TGO interface calculated by finite element analysis for the two cooling scenarios: (a) with only back side cooling and (b) with back and front sides cooling

Figure 11. Stress distributions in the coating calculated by finite element analysis and measured by Raman spectroscopy (a) for specimens cooled only from the back side and (b) for specimen cooled from both sides at the last cycle. The calculated

stresses at high temperature (HT) represent those immediately after the temperature of the coating surface drops.

Figure 12. Apparent residual stress distribution measured by Raman spectroscopy when a constant stress-free Raman peak shift is used in the calculation: (a) for specimens cooled only from the back side and (b) for specimen cooled from both sides at the last cycle.

Table 1. Material properties used in finite element simulation [21-26]

Material	T (^{o}C)	E (GPa)	ν	Yield strength (MPa)	Density (kg/m^3)	CTE (ppm/^{o}C)	Thermal conductivity (W/m.K)	Specific heat (J/kg.K)
IN-738	25	202	0.3	953	8500	11.44	8.72	428
	650	165		817		14.44	19.66	594
	800	156		789		15.16	22.28	636
	900	150		555		15.64	24.03	675
	1000	144		344		16.12	25.78	727
NiCoCrAlY	25	152	0.3	868	7320	12.59		
	500	136		807		14.33	21	628
	600	133		562		14.97		
	700	128		321		15.64		
	800	117		191		16.30		
	900	100		92		16.94	24	674
	1000	74		52		17.51		
	1100	41				17.99	34	712
TGO	25	360	0.25		3970	8.00	20.00	790
	1000			100				
	1300			100				
8YSZ	25	50	0.25		5100	10.00	0.70	479
	500					9.64	0.70	445
	1000					10.34	0.70	445

Table 2. Creep properties of materials [21, 25-26]

Material	A (s^{-1}.MPa^{-n})	Q (kJ/mol)	n
NiCoCrAlY	10^{12}	500	3
TGO	6.8×10^3	424	1
8YSZ	10^{10}	625	4
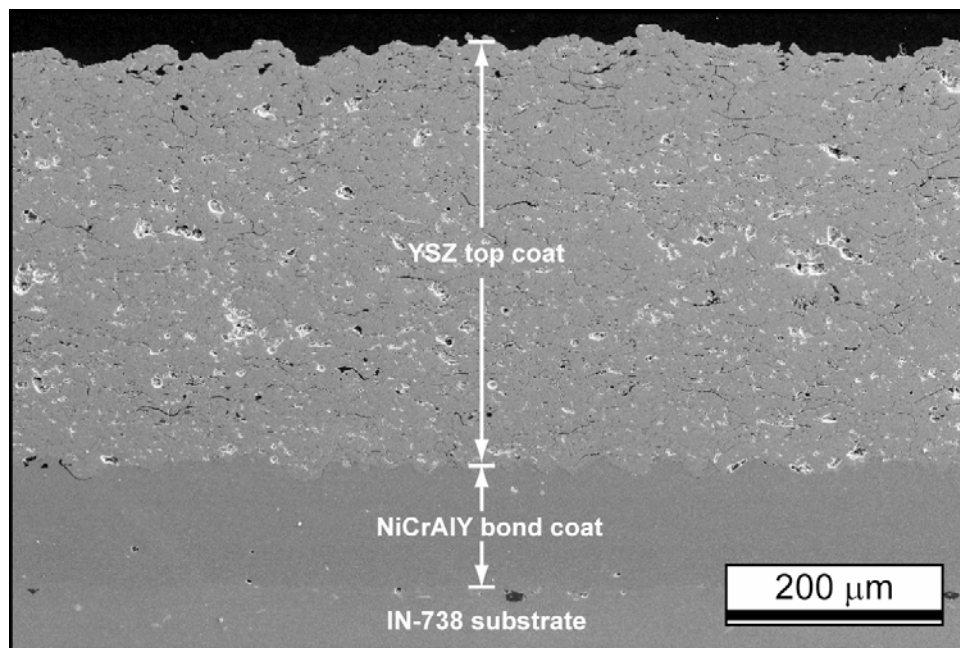
Figure 1. Limarga *et al.*
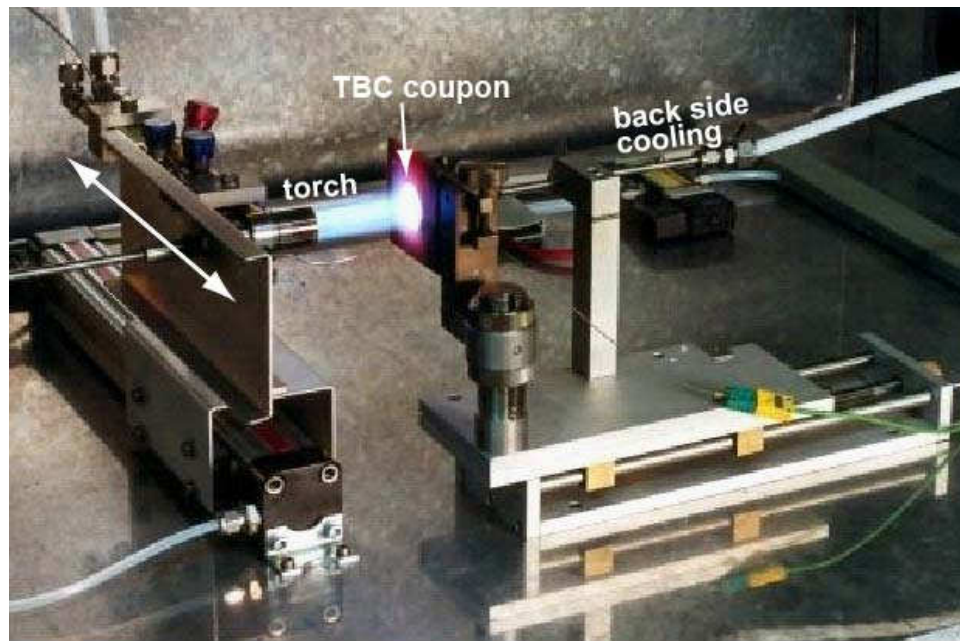
Figure 2. Limarga *et al.*
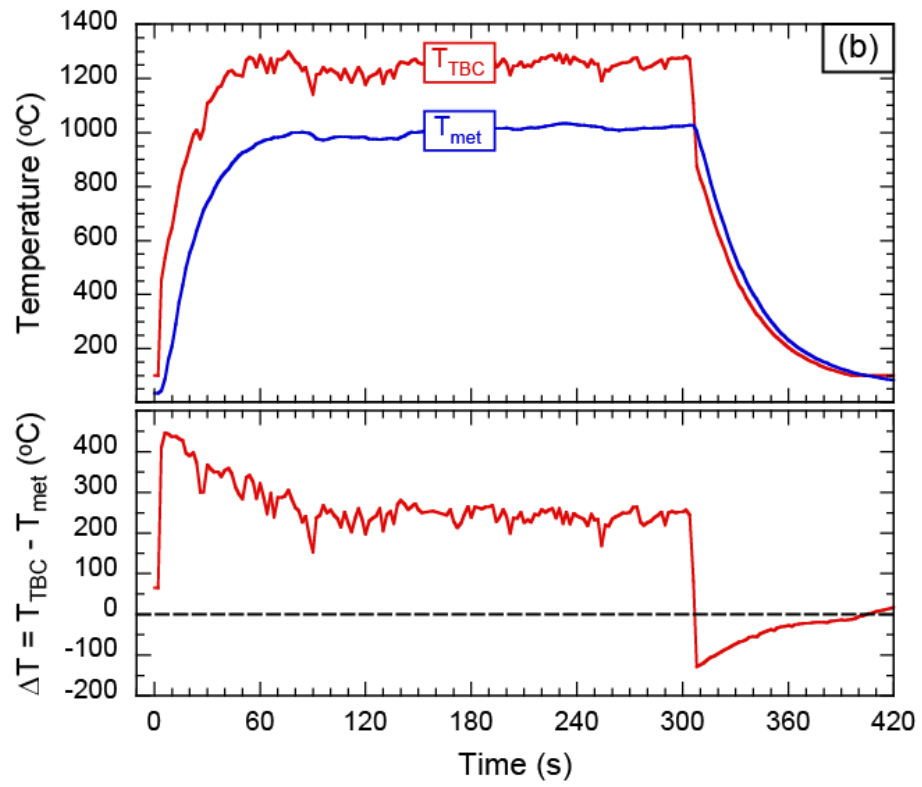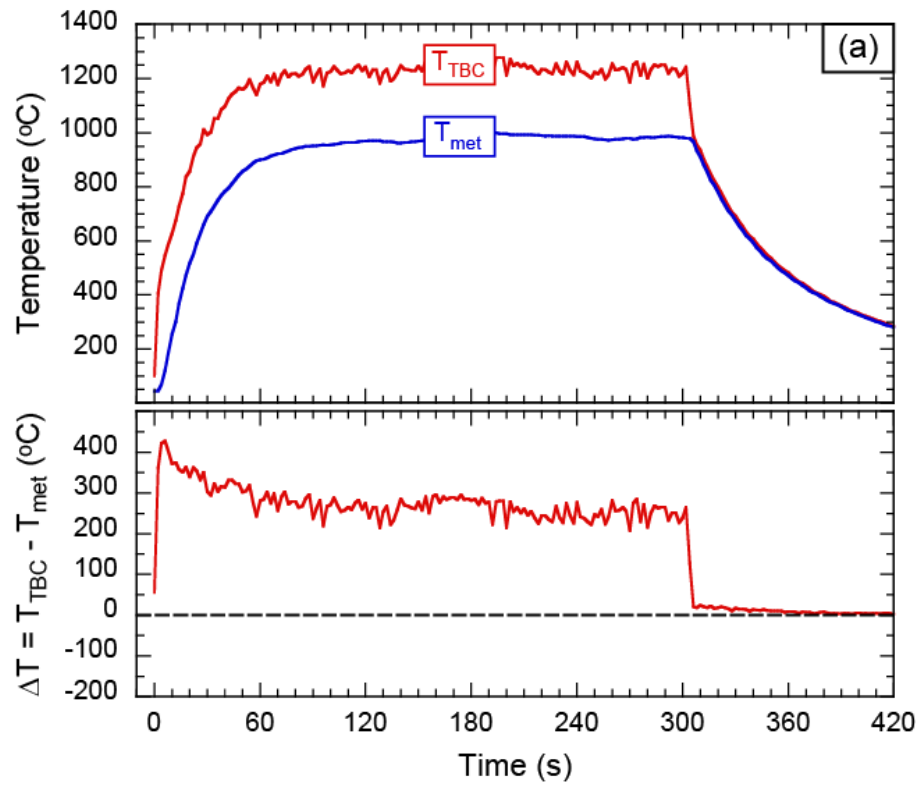
Figure 3. Limarga *et al.*
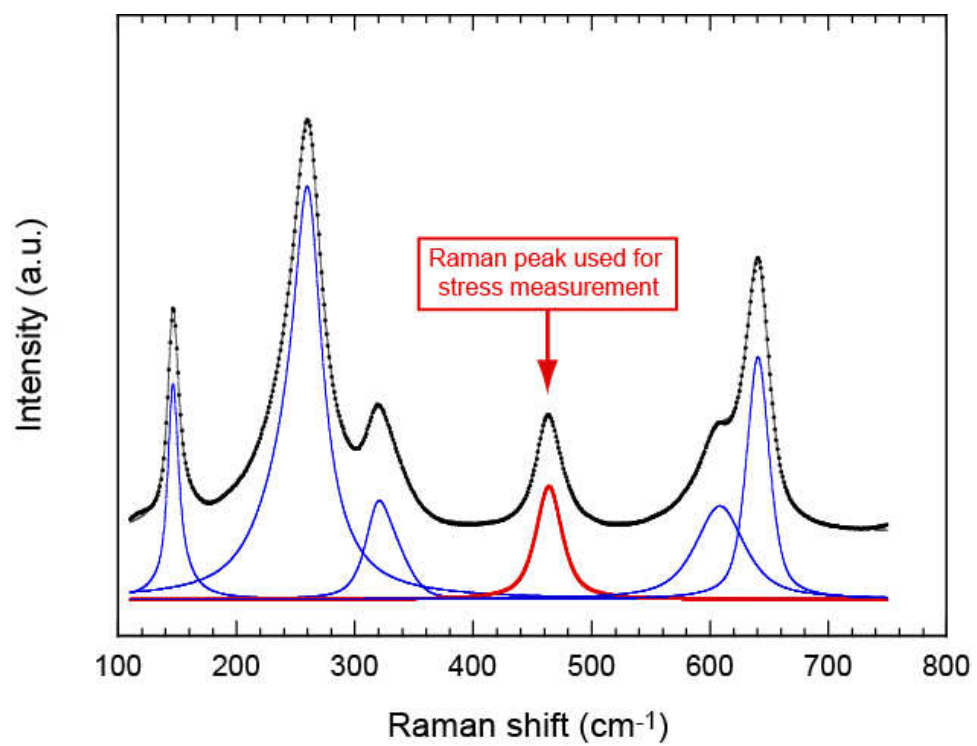
Figure 4. Limarga *et al.*
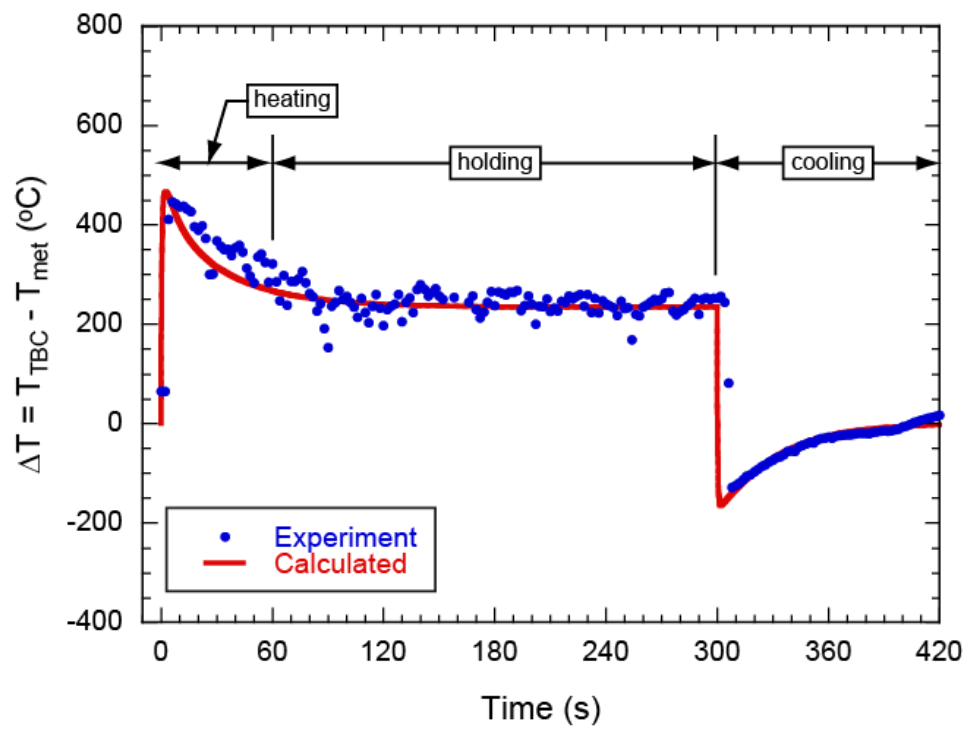
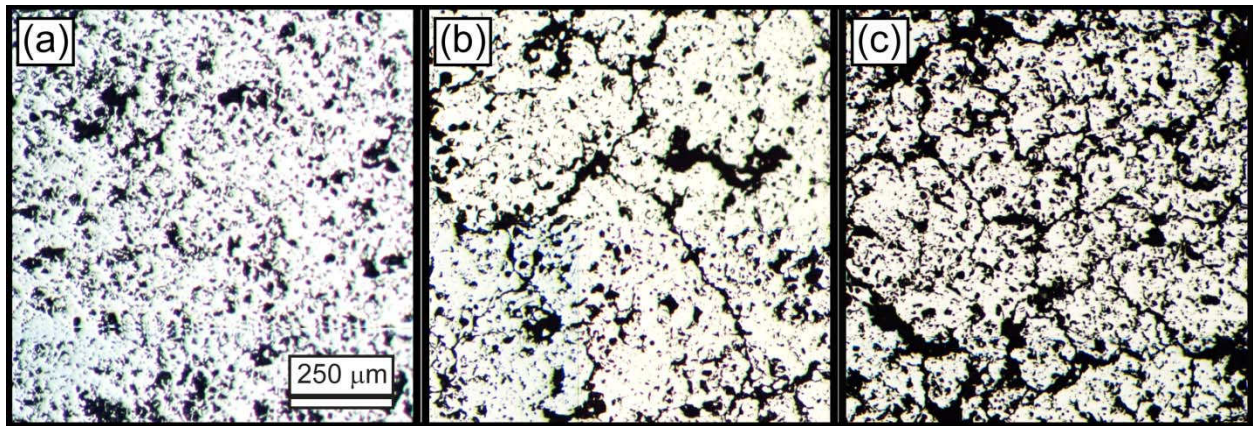Figure 5. Limarga *et al.*

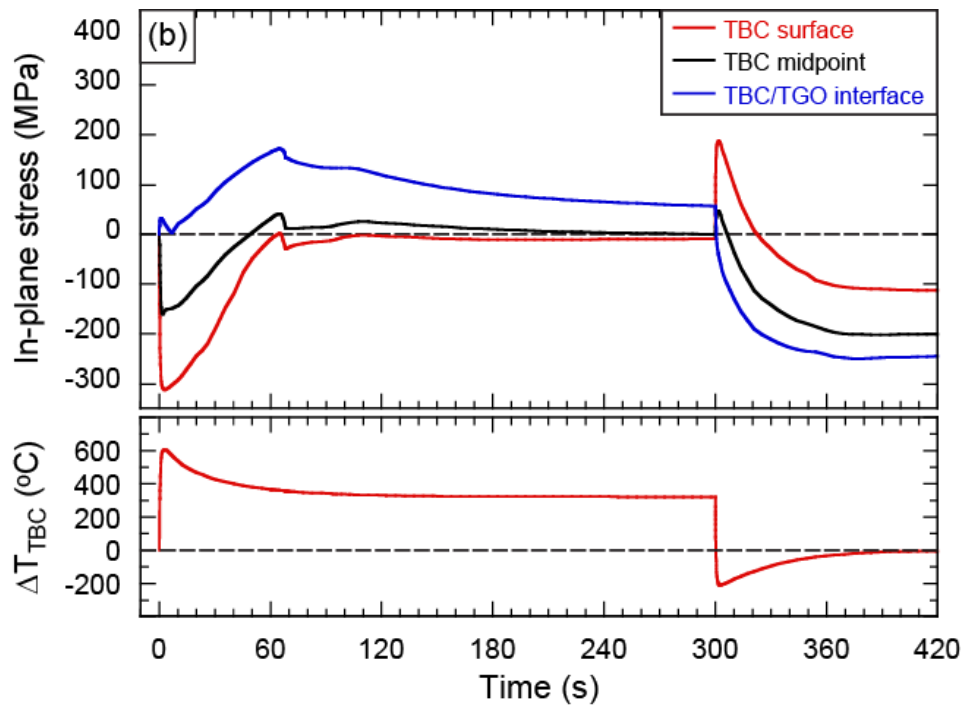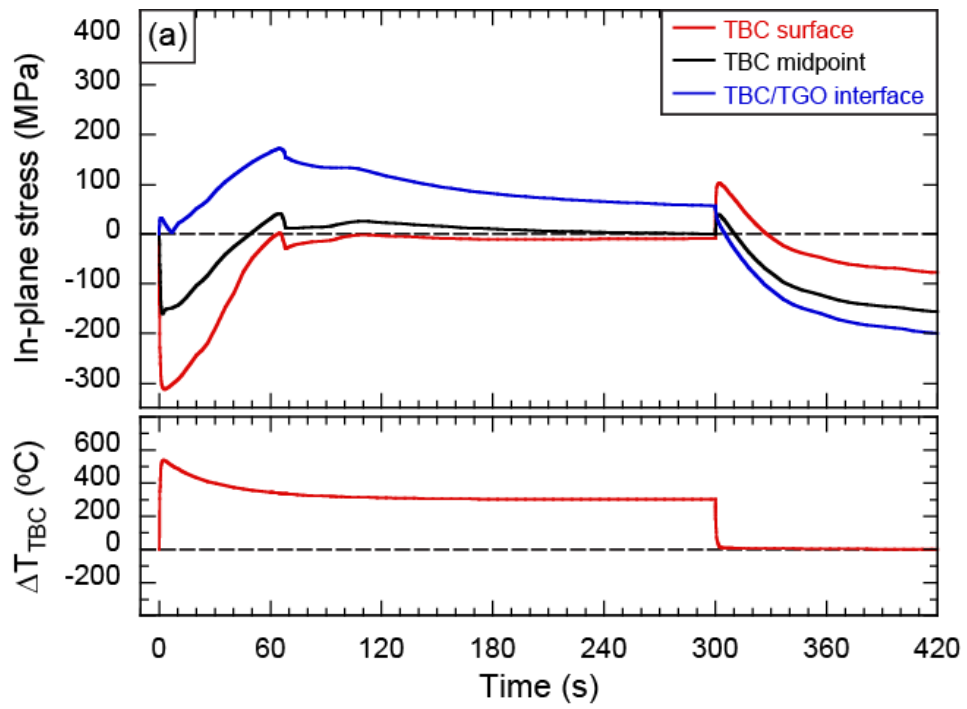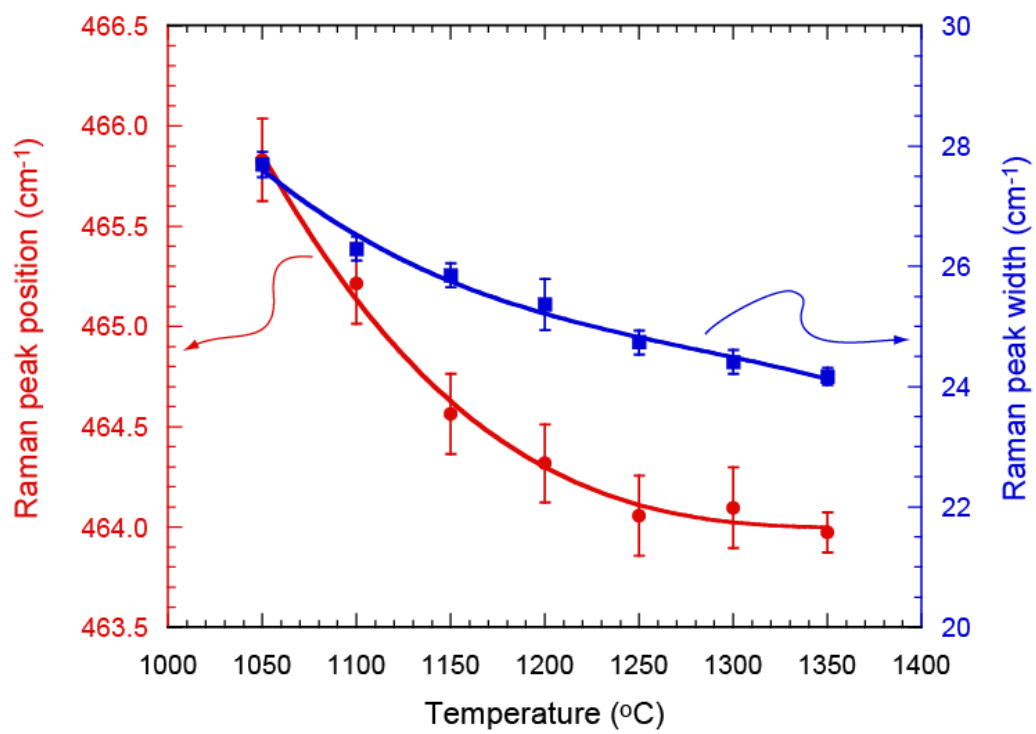Figure 6. Limarga *et al.*

Figure 7. Limarga *et al.*
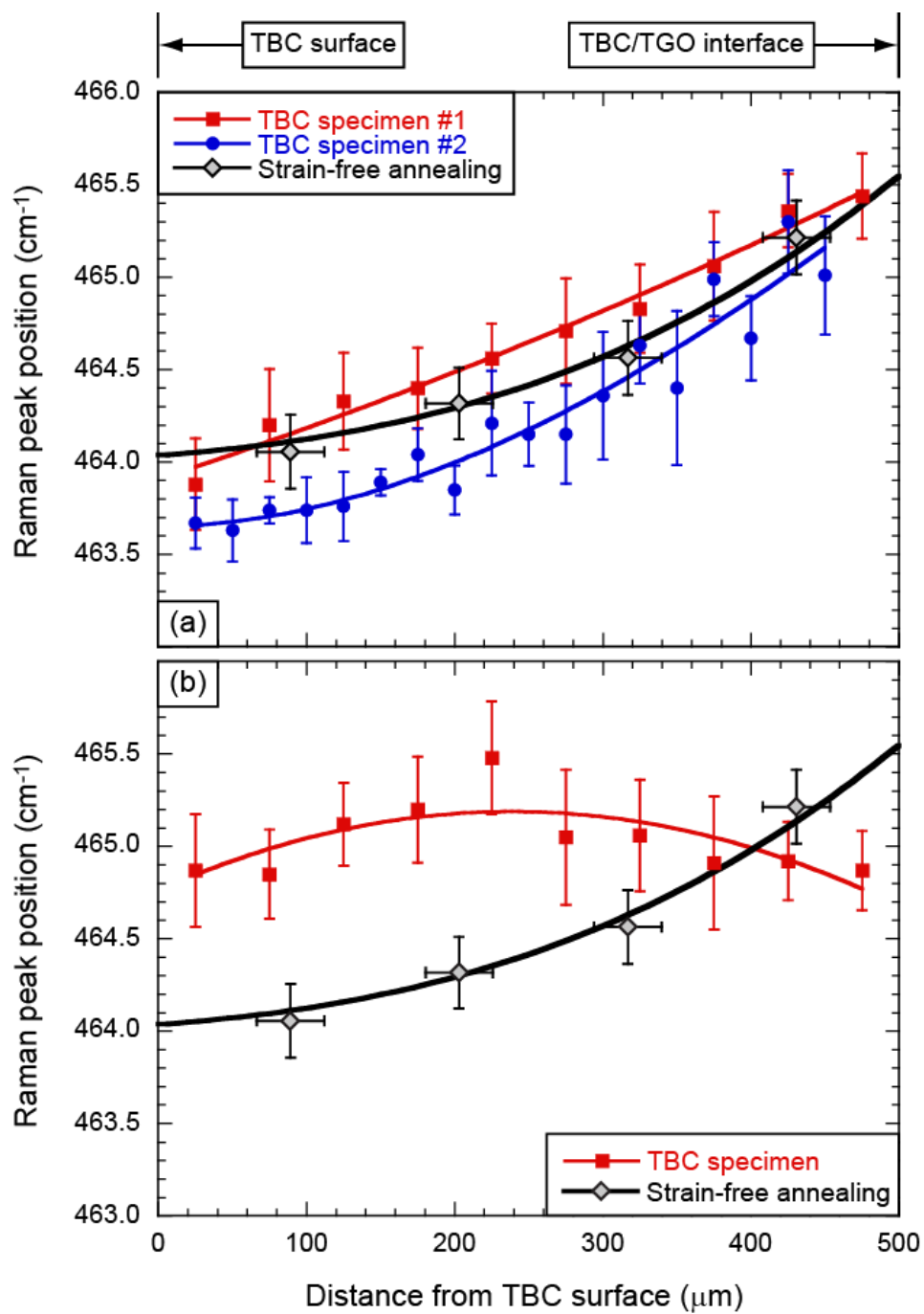
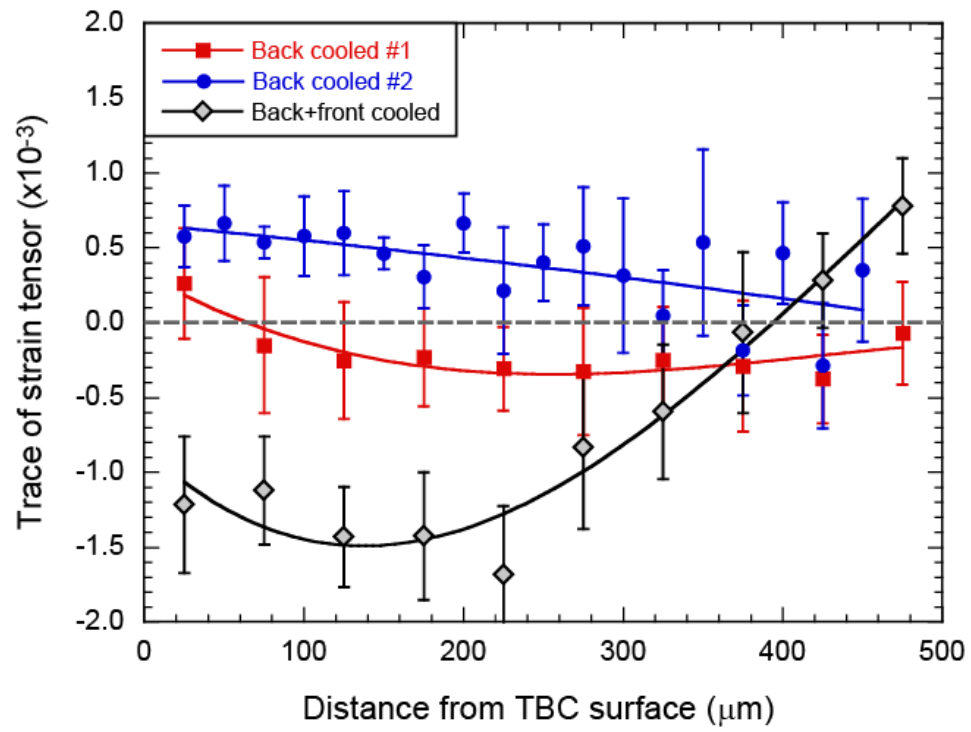Figure 8. Limarga *et al.*

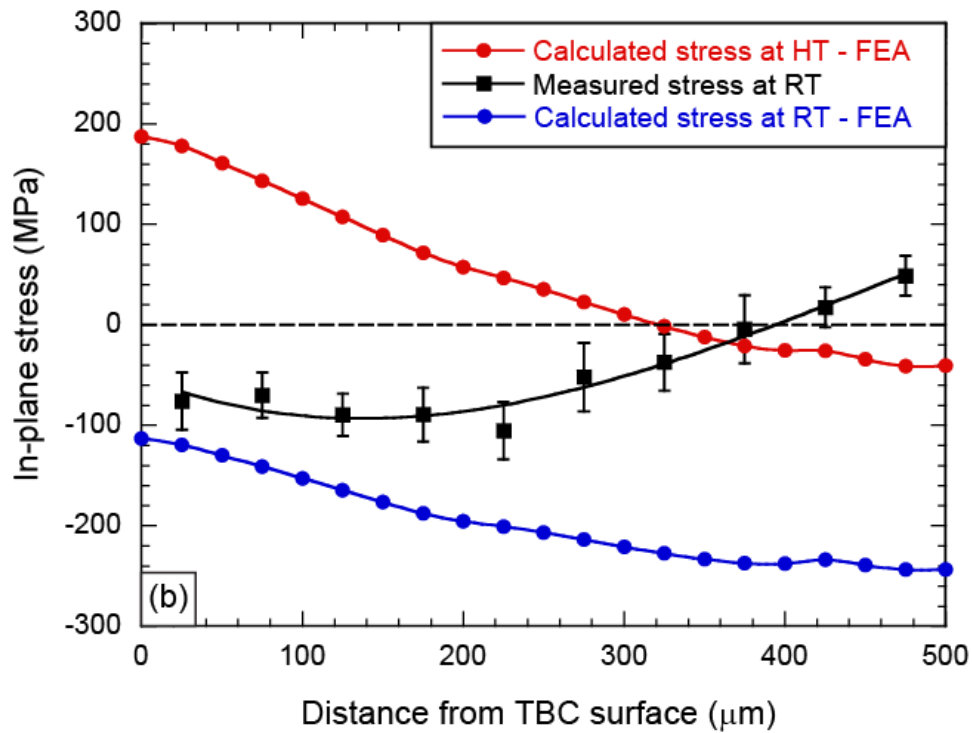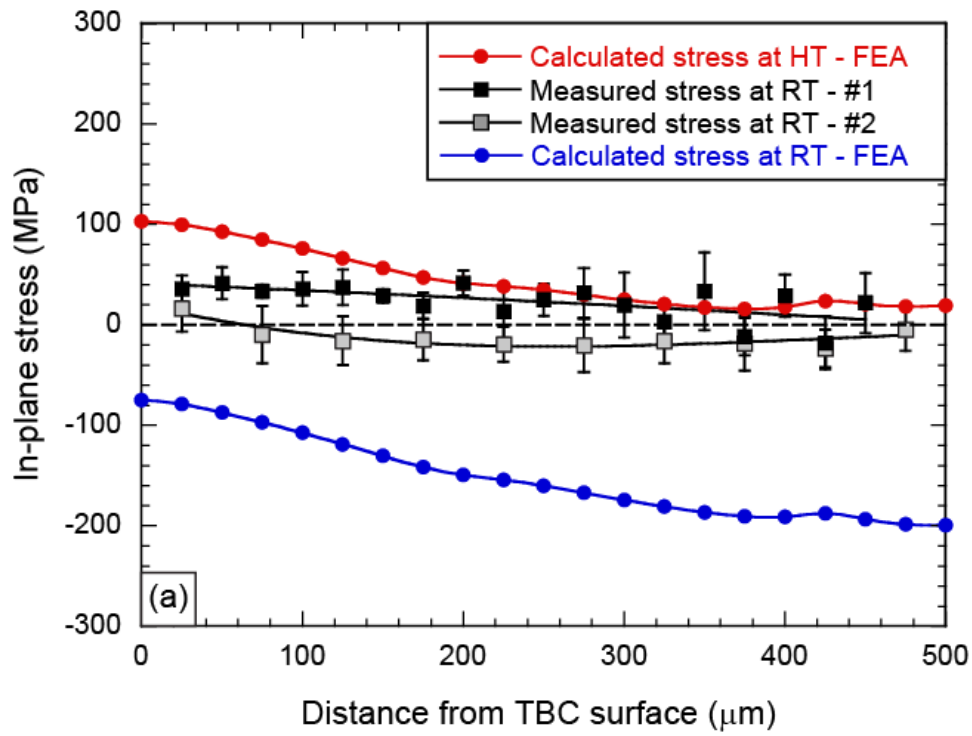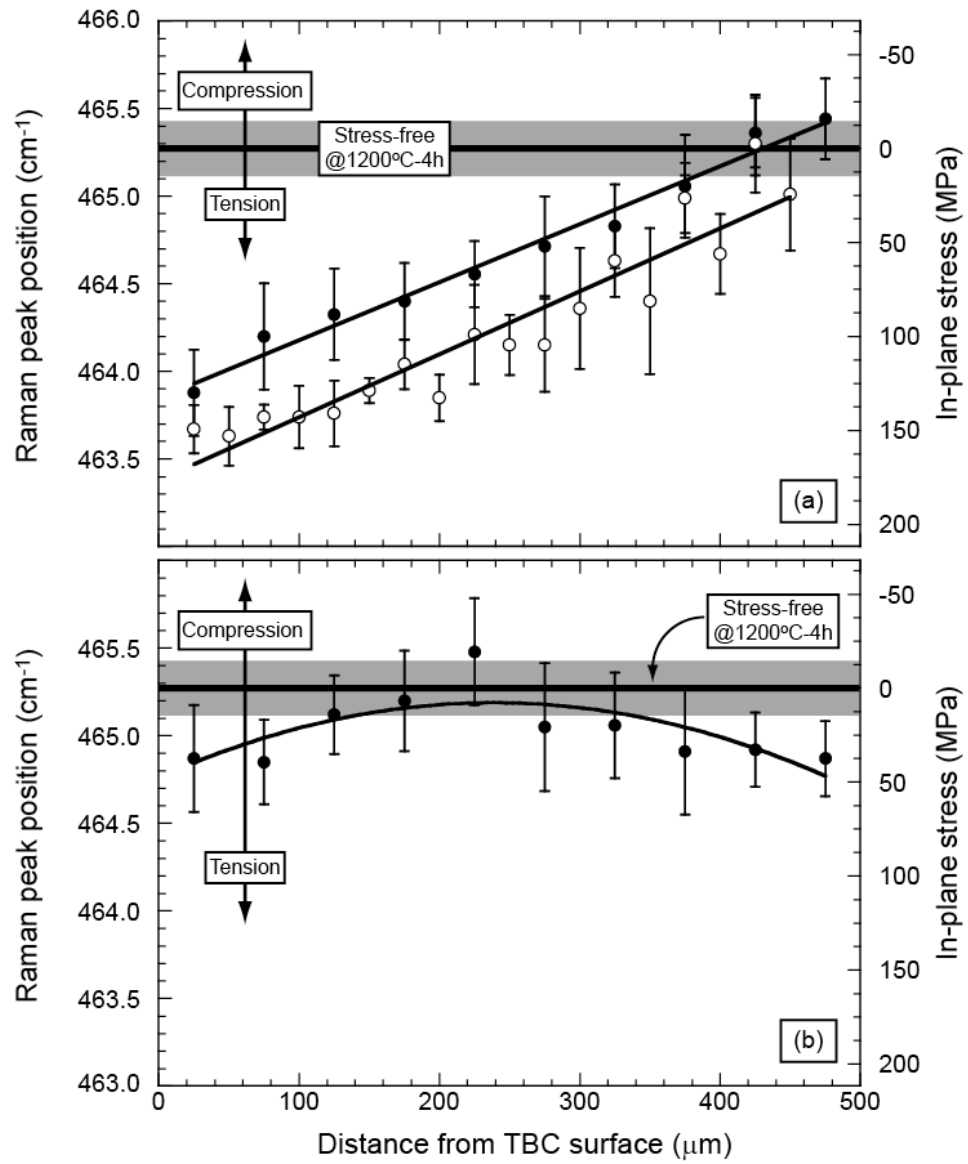Figure 9. Limarga *et al.*

Figure 10. Limarga *et al.*

Figure 11. Limarga *et al.*

Figure 12. Limarga *et al.*